J Therm Spray Tech (2019) 28:417–432
https://doi.org/10.1007/s11666-018-0820-1



PEER REVIEWED

# Thermal Shock Resistance of Thermal Barrier Coatings with Different Surface Shapes Modified by Laser Remelting

**Panpan Zhang[1,2] · Fuhai Li[2] · Xiaofeng Zhang[2] · Zhihui Zhang[1,3] · Feifei Zhou[2,4] · Luquan Ren[1] · Min Liu[2]**

Submitted: 13 June 2018 / in revised form: 4 November 2018 / Published online: 19 December 2018


**Abstract** Inspired by the unique structures and shapes of biological organisms, thermal barrier coatings (TBCs) with different shapes including dot, striation and grid were modified by laser remelting. NiCrAlY/$ZrO_2$-7 wt.%$Y_2O_3$ double-layer-structured TBCs were prepared. The microstructure, microhardness, phase composition and thermal shock behaviors of the as-sprayed and laser-treated specimens with different shapes were examined. The results indicated that the unit was characterized by the dense columnar crystal structure and the high microhardness. The thermal cycle lifetime of the dotted specimen was about twice that of the as-sprayed specimen. On the one hand, due to the elimination of defects and higher hardness after laser remelting, the dotted unit could resist thermal crack propagation. On the other hand, the columnar grains and segmented cracks in the dotted units were beneficial to increase the strain tolerance. However, due to more continuous segmented cracks and transverse cracks, the striated and grid specimens had relatively poor thermal shock resistance.

**Keywords** laser remelting · surface shape · thermal barrier coatings · thermal shock resistance

## Introduction

Thermal barrier coatings (TBCs) are widely applied to the surface of hot components in gas turbine engines, which can increase the allowable working temperature of metal components, enhance the high temperature resistance of hot components, prolong the service life of hot parts and improve the efficiency of the engine (Ref 1, 2). A typical double-layer TBCs system, which is composed of a thermally insulating ceramic top coating and an oxidation-resistant metallic bond coating, is widely used in industry. Due to its low thermal conductivity, high phase stability and high thermal expansion coefficient, the yttria partially stabilized zirconia (6-8 wt.%YSZ) ceramic has been used as top coating material for decades. MCrAlY (M/Ni, Co and Ni + Co) is usually used as the bond coating material owing to its good oxidation resistance (Ref 3). During the high-temperature service, a thermally grown oxide (TGO) layer is formed between the bond coating and the ceramic top coating due to the oxygen diffusion through the ceramic top coating (Ref 4). The TGO is mainly composed of $Al_2O_3$ and some other oxides, such as chromia ($(Cr, Al)_2O_3$), spinel ($Ni(Cr, Al)_2O_4$) and nickel oxide (NiO) (Ref 5).

Air plasma spraying (APS) and electron beam physical vapor deposition (EB-PVD) methods have been used

✉ Zhihui Zhang
zhzh@jlu.edu.cn

1 The Key Laboratory of Bionic Engineering, Ministry of Education, Jilin University, 5988 Renmin Street, Changchun 130022, China

2 National Engineering Laboratory for Modern Materials Surface Engineering Technology, the Key Lab of Guangdong for Modern Surface Engineering Technology, Guangdong Institute of New Materials, Guangzhou 510651, China

3 The State Key Laboratory of Automotive Simulation and Control, Jilin University, 5988 Renmin Street, Changchun 130022, China

4 Laboratory of Nano Surface Engineering, Department of Materials Science, School of Materials Science and Engineering, Harbin Institute of Technology, Harbin 150001, China

extensively for the deposition of top ceramic coating (Ref 6-8). However, the capital cost of setting up a commercial EB-PVD plant is high. By contrast, APS is widely used in industry due to its many advantages such as low thermal conductivity coatings, low cost and good chemical stability under high temperature (Ref 9-11).

Plasma-sprayed TBCs have a relatively short thermal cycle lifetime, which is often the result of the synergistic action between various factors, such as the thermal expansion coefficient mismatch between the coating and the metallic substrate, the formation of TGO at the bond coating/top coating interface and phase transformation of zirconia from tetragonal to monoclinic during thermal cycles (Ref 12-15). So far, many studies have focused on the improvement in thermal shock resistance. Soleimanipour et al. conducted the laser cladding of alumina on the top surface of YSZ thermal barrier coatings and found that the thermal shock resistance was improved after laser cladding (Ref 16). Ghasemi et al. revealed that the laser glazing process produced network cracks perpendicular to the surface and finally improved the thermal shock resistance of nanostructure thermal barrier coatings (Ref 17). Fan et al. investigated the influence of columnar grain morphology on the thermal shock resistance of laser-remelted YSZ thermal barrier coatings and showed that columnar grains with small size were beneficial to the thermal shock resistance (Ref 18). Therefore, laser technology is a promising method to improve the thermal shock resistance of TBCs, which can remove the pores and microcracks of the plasma-sprayed TBCs and provide a dense layer containing segmented cracks (Ref 16-18). Moreover, the segmented cracks produced by laser are beneficial to accommodate the oxidation and mismatch stresses, finally leading to the extension of thermal shock lifetime of TBCs (Ref 19). Nevertheless, the conventional laser treatment processes the whole ceramic top coating, which may generate the high-level residual stresses in the whole coating and form a new weak interface between the laser-treated layer and the remained layer.

In nature, some animals and plants (Ref 20-23) develop their own unique structures and shapes, which endow them with excellent performance in comparison with man-made materials. The superior performance is often the result of the coupling effect between various factors, such as surface morphology, internal microstructure, material composition. Usually, there are some functional units existing within the surface layer of organisms which are different from the basal body in those factors. These basic functional units are crucial to understanding the excellent performance of biological materials. In terms of the unit shapes, Ren et al. reported that there were generally three typical structural shapes of functional units in biological organisms, namely dot, striation and grid, which could provide them with excellent biomechanical properties against the harsh environment (Ref 24-26); their biological prototypes are shown in Fig. 1. Song et al. studied the crack evolution in the nacreous layer with brick-and-mortar structure and found that the crack deflection was occurred by constrained microcracking, thus enhancing the crack extension resistance (Ref 27). Zhang et al. observed the crack initiation and the dynamic propagation process of dragonfly wing and found that dragonfly veins had a crack arrest effect in the crack propagation process (Ref 28). Therefore, those functional units can extend the crack propagation path and time, thereby providing an excellent crack arrest function (Ref 27, 28). In fact, the failure of TBCs is governed by a sequence of crack initiation, propagation and coalescence, leading to the spallation of coating (Ref 29, 30). Therefore, the principle of biomimetics can be introduced into the thermal barrier coatings to solve problems. The biomimetic laser remelting is that laser remelts the coating with specific pattern inspired from nature, which is completely different from the conventional laser remelting that laser remelts the whole ceramic top coating. The biomimetic laser remelting method can not only make the best use of

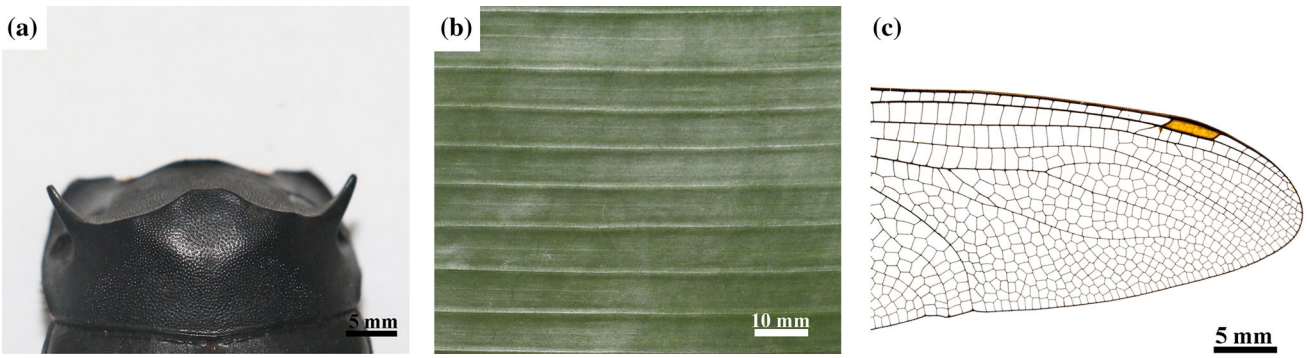


**Fig. 1** Typical structural shapes of functional units in biological organisms: (a) dotted units in the postnotum of dung beetle, (b) striated units in the tree leaf, and (c) grid units in the dragonfly wing

the advantages but also avoid the disadvantages of conventional laser remelting. Due to the relative low cost and high efficiency, the biomimetic laser remelting is an alternative approach to the industrial application of TBCs. Although Chang et al. investigated the thermal shock resistance of peg-nail-structured or dotted TBCs (Ref 31), they focused on the effect of laser parameter on the thermal shock behaviors. However, the thermal shock behaviors of TBCs with different surface shapes processed by laser remelting have few reports.

In this study, double-layer-structured NiCrAlY/$ZrO_2$-7 wt.%$Y_2O_3$ TBCs were fabricated. Specimens were made with three types of morphologies, namely dot, striation and grid, which were obtained by laser remelting using Nd:YAG laser. The effects of laser remelting on the microstructure, microhardness, phase composition and thermal shock resistance of the plasma-sprayed TBCs were studied. Experiments were focused on the effects of unit shape on the thermal shock behavior of the bio-inspired TBCs. The thermal shock failure mechanisms were also investigated.

## Materials and Methods

### Material

Nickel-based superalloy K417G was used as the substrate with a dimension of 25.4 mm in diameter and 6 mm in thickness. The coating materials were commercially available NiCrAlY powder (AMPERIT 413, H.C. Starck, Germany) with particle size of 5-45 μm (Fig. 2a) and $ZrO_2$-7 wt.%$Y_2O_3$ (7YSZ) powder (AMPERIT 827, H.C. Starck, Germany) with particle size of 10-45 μm (Fig. 2b). In order to increase adherence capability, the superalloy substrate was grit-blasted. After grit blasting, the NiCrAlY bond coating with a thickness of about 100 ± 10 μm was firstly sprayed on the superalloy substrate by using the low-temperature high-velocity oxygen fuel (LT-HVOF) spraying system (K2, GTV, Germany), and then the 7YSZ ceramic coating with a thickness of about 200 ± 10 μm was sprayed on the bond coating by means of air plasma spraying (APS) system (MF-P 1000, GTV, Germany). Spraying conditions of the bond coating and the YSZ coating are listed in Tables 1 and 2, respectively.

### Laser Process

A pulsed Nd:YAG laser (XL-1000Y, China) with maximum power of 1000 W and wavelength of 1064 nm and Gaussian distribution was used for processing different surface shapes on the specimens. The laser process parameters were listed as follows: the input energy of 4 J, the pulse duration of 5 ms, the frequency of 1 Hz and the laser spot diameter of approximately 1.4 mm. The surface images of the as-sprayed and laser-treated specimens with different shapes are shown in Fig. 3. Here, the area ratio is defined as the ratio of the sum surface area of laser-treated zone to the whole surface area of specimen. Table 3 shows the area ratio of the laser-treated specimens with different shapes.

**Table 1** Spraying parameters of LT-HVOF for bond coatings

| Parameter | NiCrAlY |
|---|---|
| Spray distance, mm | 150 |
| Kerosene, L/h | 13 |
| Oxygen, L/min | 750 |
| Chamber pressure, bar | 14.9 |
| Powder feed rate, g/min | 40 |
| Gun speed, mm/min | 1000 |
| Overlap distance, mm | 6 |

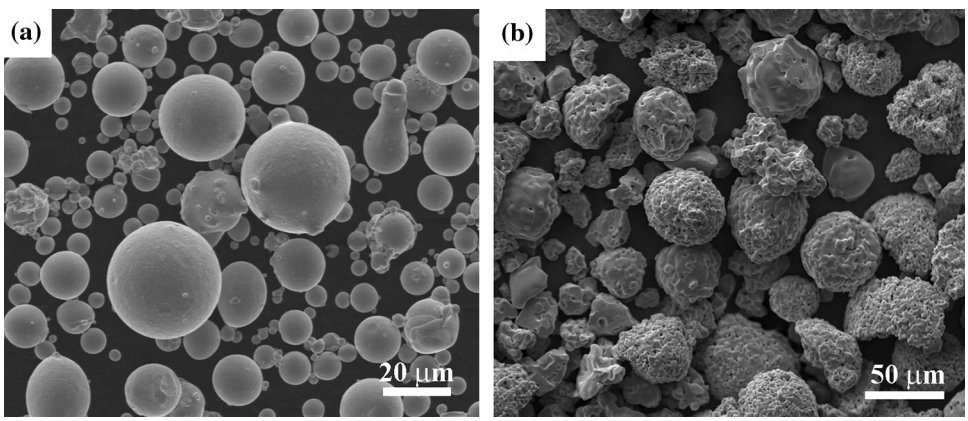


**Fig. 2** Morphologies of powders: (a) NiCrAlY used in metallic bond coating, and (b) 7YSZ used in ceramic top coating

### Thermal Shock Test

In order to shorten the experimental time, thermal shock test was performed by heating and the water quenching method (Ref 31, 32). During the water cooling process, water evaporated quite rapidly and the formed water vapor might damage the coatings. This might deteriorate the oxidation of bond coating and facilitate the growth of the TGO layer, which finally could accelerate the failure of TBCs. Both the as-sprayed and the laser-treated specimens with different shapes were heated to 1000 °C and maintained for 5 min in an electric resistance furnace, and then the heated specimens were immersed into deionized water bath which was maintained at 25 °C. When the specimens were cooled to the ambient temperature, they were taken out, dried and put into the high-temperature furnace again, repeating the same process. When the TBC spallation area reached about 20% of the total coating surface, the test was stopped and the number of thermal shock cycles for each specimen was recorded. Three specimens were tested to obtain the average value of thermal shock lifetime.

**Table 2** Spraying parameters of APS for ceramic coatings

| Parameter | YSZ |
|---|---|
| Current, A | 650 |
| Voltage, V | 70 |
| Primary gas, Ar (SLPM) | 45 |
| Second gas, $H_2$ (SLPM) | 9 |
| Carrier gas, Ar (SLPM) | 4 |
| Spray distance, mm | 110 |
| Powder feed rate, g/min | 60 |
| Gun speed, mm/min | 1000 |
| Overlap distance, mm | 6 |

**Table 3** Area ratio of the laser-treated specimens with different shapes

| | Area ratio, % |
|---|---|
| Dotted specimen | 18 |
| Striated specimen | 26 |
| Grid specimen | 58 |

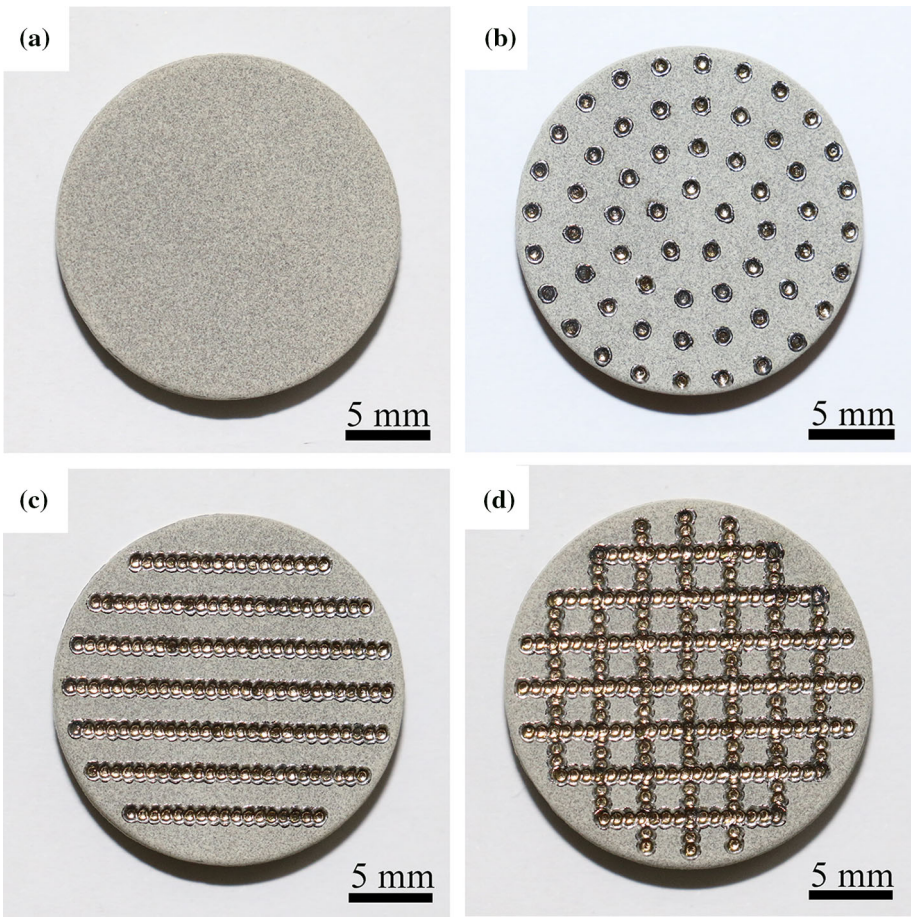


**Fig. 3** Surface images of specimens: (a) as-sprayed specimen, (b) dotted specimen, (c) striated specimen, and (d) grid specimen

## Characterization

The microstructures of the powders, as-sprayed and laser-treated TBCs with different shapes were characterized via a scanning electron microscopy (SEM) (SU8220, Hitachi, Japan) equipped with energy dispersion spectroscopy (EDS). The TGO thickness was, respectively, measured ten times using SEM, and then the mean value was achieved as the experimental result. The SEM images were captured at different areas in the cross-sectional coating, and the porosity in the coatings was determined by measuring the pixels associated with the difference in contrast, from the SEM images by using ImageJ software. The porosity reported is the average of fifteen values. The phase compositions of the powder, as-sprayed and laser-treated specimens with different shapes were identified using the x-ray diffractometer (XRD), employing Cu K$\alpha$ radiation. The x-ray generator was operated at 40 kV and 100 mA at a $2\theta$ range of 10°-90° with scanning speed of 4°/min. In order to identify the existence of monoclinic zirconia, a slow scan at the $2\theta$ range of 27.5°-32.5° with scanning speed of 0.2°/min was conducted. The microhardness was tested by the Vickers hardness tester (MH-5D, China) under a load of 100 g for 10 s. The hardness values in the polished cross section of remelted zone were averaged by fifteen points of measurements.

## Results and Discussion

### Surface Morphology and Microstructure

Figure 4 shows the surface morphologies of the as-sprayed and laser-treated TBCs with different shapes. It should be noted that different TBCs show the obviously different surface morphologies. The surface of the as-sprayed coating, depicted in Fig. 4(a), presents some microcracks, pores, voids and protrusions, which is a typical phenomenon for the plasma-sprayed 7YSZ TBCs. The microcracks formed in the ceramic top coating are due to the induced thermal stress caused by rapid cooling (cooling rates in the range of $10^6$-$10^8$ K/s) (Ref 33). The surface morphologies of laser-treated specimens with different shapes are presented in Fig. 4(b), (c) and (d). After the laser treatment, the surface of laser-treated zone becomes relatively smoother than that of the as-sprayed coating. Meanwhile, the defects such as pores, microcracks, protrusions in the as-sprayed coatings are eliminated. It is interesting that the surface of laser-treated zone all exhibits the typical segmented cracks, whose width is about 2-6 μm, as shown in Fig. 4(b), (c) and (d). The formation of segmented cracks can be ascribed to the volume shrinkage and relaxation of residual stresses during the rapid and non-uniform cooling of molten zirconia (Ref

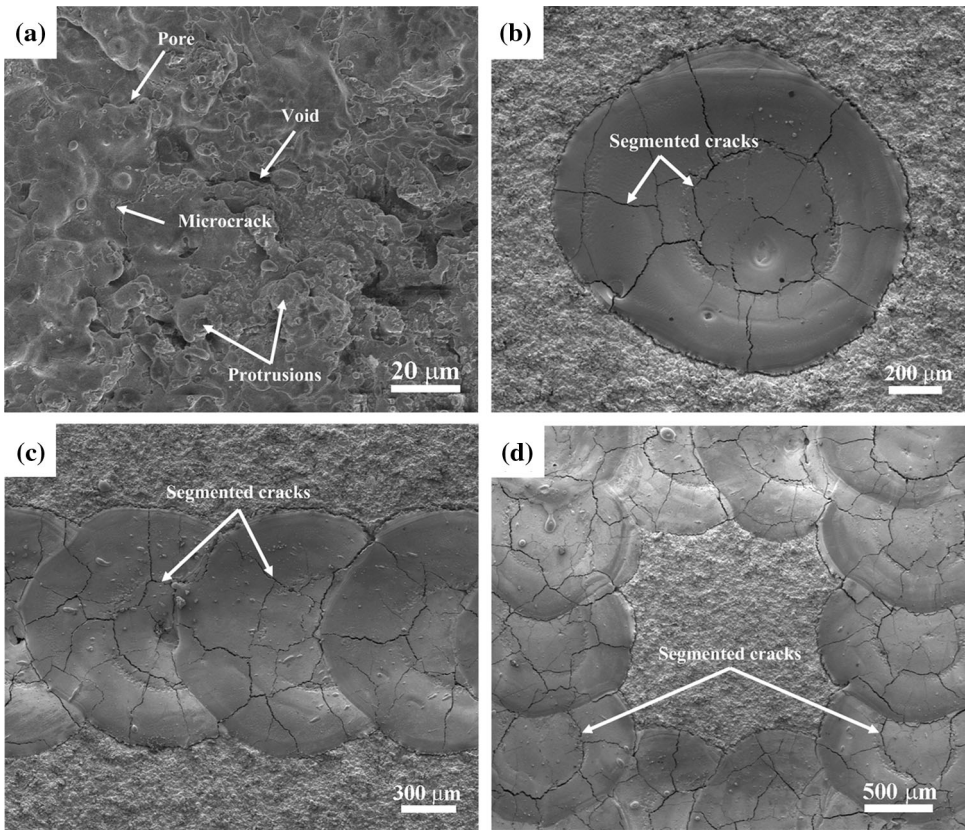


**Fig. 4** Surface morphologies of specimens: (a) as-sprayed TBC, (b) dotted TBC, (c) striated TBC, and (d) grid TBC

31, 34) and probably the large and localized temperature gradient, which generates residual stresses after the laser treatment.

Figure 5(a) presents the cross section of as-sprayed TBC, which is composed of the YSZ top coating and NiCrAlY bond coating deposited on the superalloy substrate. It can be seen from Fig. 5(b) that there are many voids and microcracks in the ceramic coating, which has the porosity of approximately 14.8 ± 3.0%. This is mainly due to the insufficient overlapping among the adjacent splats and the entrapped gas during the plasma spraying process; thus, the pores and voids are formed in the ceramic coating. As depicted in Fig. 5(c), the plasma-sprayed ceramic coating presents the typical lamellar structure. During thermal spraying, 7YSZ powders are carried into the plasma plume by the inert gas mixture, and they are melted and accelerated in the plasma flame; then, the molten particles impact and solidify on the substrate, and the later splats will be deposited onto the former splat (Ref 35); hence, the characteristic lamellar microstructure is formed in the ceramic coating.

The cross-sectional morphologies of the laser-treated TBCs are presented in Fig. 6. After the laser treatment, the zone where the microstructure is different from the ceramic coating comes into being in the surface layer of coating. The zone is defined as bionic unit (Fig. 6a), which consists of two characteristic microstructure zones, i.e., remelted zone and heat-affected zone (HAZ). The width of the bionic unit is approximately 1.2 mm, and the depth is about 161 μm. Under the action of laser irradiation, the YSZ material remelted and then solidified rapidly, and finally the bionic unit was formed. From Fig. 6(a), the vertical cracks which are also called segmented cracks were found in the remelted zone, and there were nearly transverse cracks around the unit. This is mainly attributed to the thermal stress induced by inhomogeneous volume shrinkage. Since the intensity profile of laser beam follows a Gaussian distribution during the laser remelting process, the center of the molten pool absorbs more energy than that of the edge part. Thus, the central part of bionic unit has higher temperature than its edge. The higher shrinkage of the central part generates tensile stresses with respect to the edge of bionic unit. As a result, the vertical cracks are formed in the remelted zone, which have proven to be very beneficial to accommodate the thermal stresses and mismatch stresses (Ref 36). It is easy to understand that the temperature of the laser-treated zone (bionic unit) is higher than that of the untreated zone. Therefore, the laser-treated zone experiences higher shrinkage during the cooling process. Finally, the nearly transverse cracks are formed around the unit. Figure 6(b) shows the microstructures of remelted zone at a higher magnification, whose porosity is about 0.5 ± 0.2%. It is obvious that the coating becomes much denser after the laser treatment and the low porosity unit is obtained. As mentioned above, a large thermal gradient will develop between the center and the edge of molten pool under laser irradiation, which further leads to the surface tension gradient and attendant Marangoni flow (Ref 37). Both the present torque and the Marangoni flow make the liquid material rotate in the molten pool. In this case, the gas can easily escape from the coating, and thus a low porosity bionic unit is achieved. The fracture microstructure of the unit exhibits the dense columnar crystal structure, as shown in Fig. 6(c). It is mainly determined by the ratio of temperature gradient to solidification rate during laser treatment. The columnar crystal structure forms in the remelted zone, which corresponds to the direction of the highest thermal gradient. Figure 6(d) shows the microstructure of the HAZ. Note that the morphologies of the HAZ are extremely different from the remelted zone. In this zone, the number of defects such as pores and microcracks reduces. Under the action of laser, there is not enough energy spreading to the HAZ due to the thermal influence from the remelted zone; hence, the pores do not have enough time to escape from the molten pool as the laser beam moves away. Consequently, the

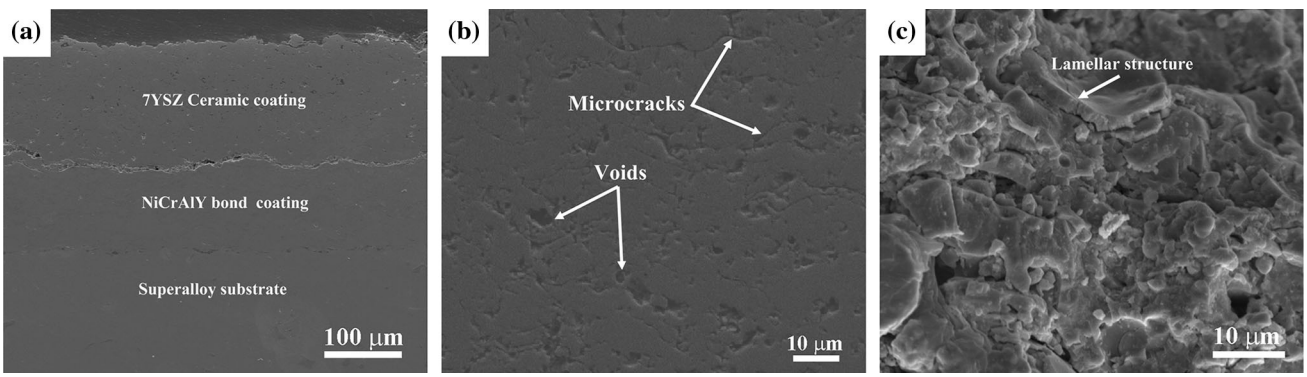


**Fig. 5** SEM photograph of (a) the polished cross section of the as-sprayed specimen, (b) ceramic coating at a high magnification, and (c) fracture cross section of ceramic coating

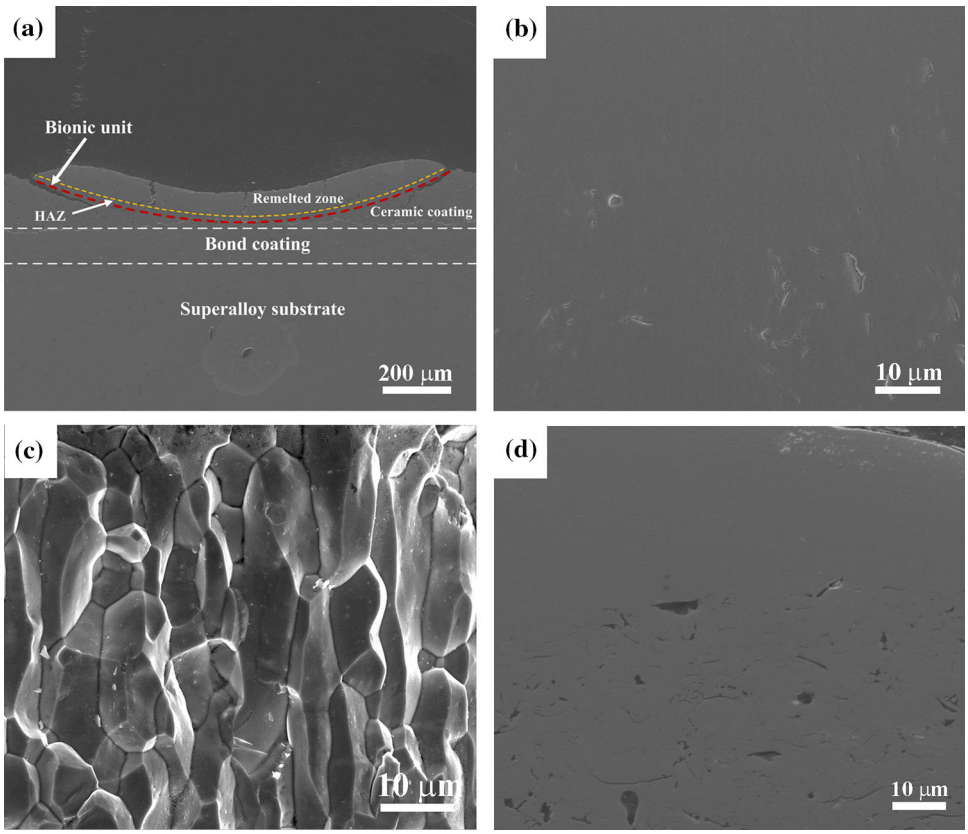


**Fig. 6** Cross-sectional morphologies of the laser-treated specimen: (a) overview of unit, (b) polished microstructure in the remelted zone, (c) fracture microstructure in the remelted zone, and (d) microstructure in the HAZ

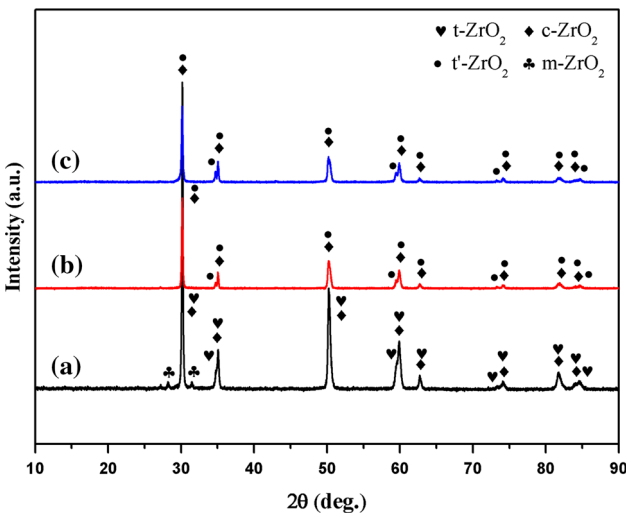


**Fig. 7** XRD diffraction patterns in the entire range: (a) 7YSZ ceramic powder, (b) as-sprayed specimen, and (c) laser-treated specimen

microstructure of the HAZ is less dense than that of the remelted region.

## Phase Composition

Figure 7 exhibits the XRD patterns of the original ceramic powder, the as-sprayed and the laser-treated TBCs at the $2\theta$ range of 10°-90°. The phases of YSZ ceramic powder consist of primary tetragonal zirconia (t-$ZrO_2$), cubic zirconia (c-$ZrO_2$) and a small amount of monoclinic zirconia (m-$ZrO_2$). However, the m-$ZrO_2$ disappears after the air plasma spraying and the laser remelting process, and all phases in the powder change to non-equilibrium tetragonal zirconia (t′-$ZrO_2$) and c-$ZrO_2$. The formation of the t′-$ZrO_2$ is due to the diffusionless phase transformation of the high-temperature c-$ZrO_2$ at high cooling rate of $10^6$ K/s (Ref 32). Due to the rapid cooling and solidification rate of air plasma spraying and laser remelting, the phase transformation of t′-$ZrO_2$ to m-$ZrO_2$ is restrained. Therefore, no m-$ZrO_2$ phase is found in the as-sprayed and the laser-treated specimens.

**Table 4** Microhardness of the as-sprayed coating and laser-remelted zone

| Specimen | Microhardness ($HV_{0.1}$) |
|---|---|
| As-sprayed coating | 793 ± 46 |
| Laser-remelted zone | 1372 ± 71 |

## Microhardness

Table 4 shows the microhardness of the as-sprayed coating and laser-remelted zone. The microhardness of the as-

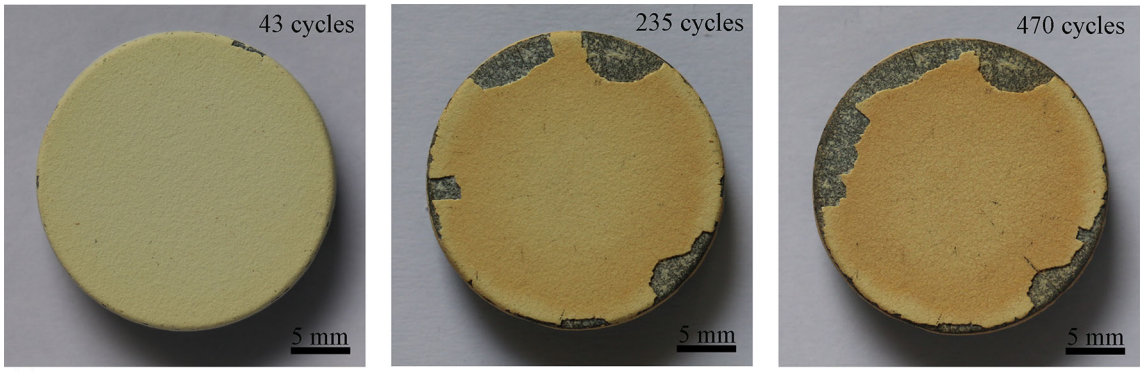
43 cycles
5 mm
235 cycles
5 mm
470 cycles
5 mm

(a)

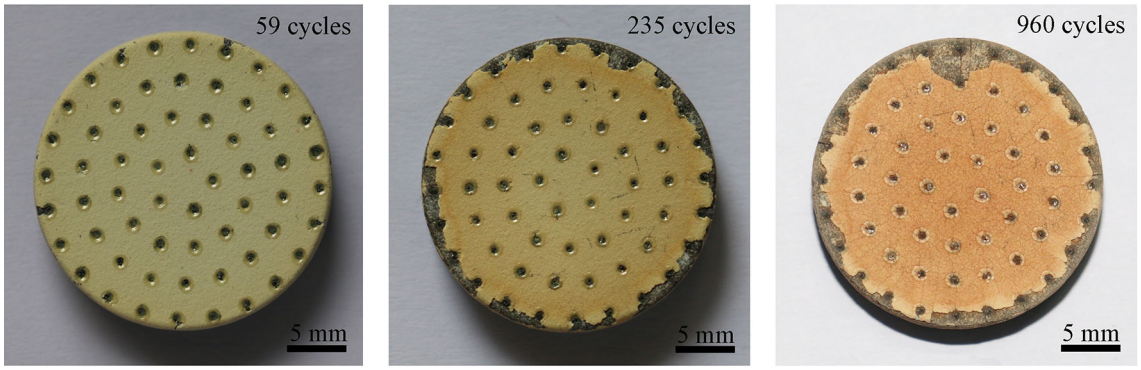
59 cycles
5 mm
235 cycles
5 mm
960 cycles
5 mm

(b)

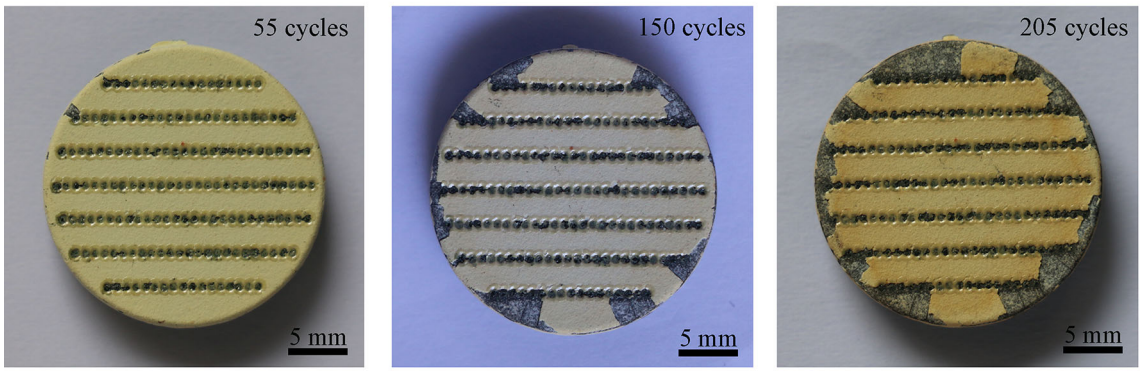
55 cycles
5 mm
150 cycles
5 mm
205 cycles
5 mm

(c)

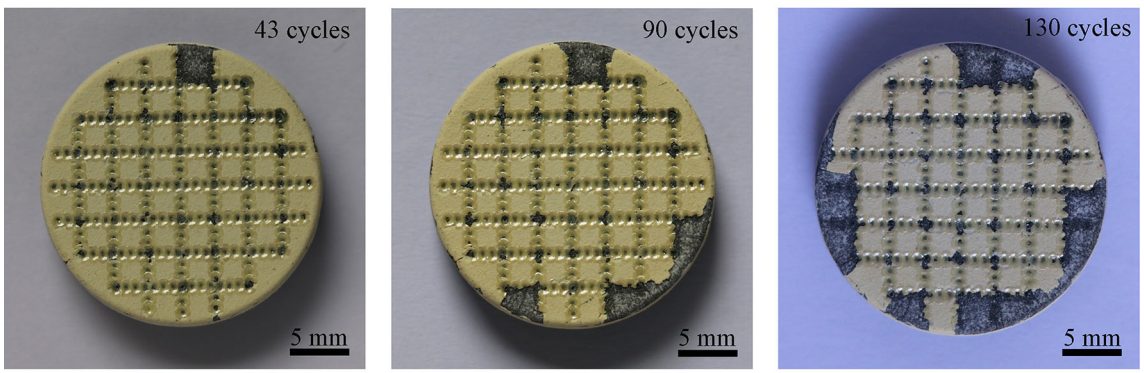
43 cycles
5 mm
90 cycles
5 mm
130 cycles
5 mm

(d)

◀**Fig. 8** Macro-photographs of specimens during thermal shock test: (a) as-sprayed specimen, (b) dotted specimen, (c) striated specimen, and (d) grid specimen

sprayed coating is about $793 \pm 46$ $HV_{0.1}$, while the microhardness value of the laser-remelted zone is $1372 \pm 71$ $HV_{0.1}$. That is to say, the microhardness is increased by 73% after laser remelting treatment. The higher microhardness of the laser-remelted zone is mainly caused by the elimination of pores and voids and the formation of dense columnar crystal structure after laser remelting treatment.

## Thermal Shock Resistance

The macroscopic photographs of the as-sprayed and laser-treated specimens with different shapes during thermal shock test are shown in Fig. 8. As can be seen, for both the as-sprayed and the laser-treated coatings with different shapes, failure or spallation of the coatings initiates from the edges of all coatings and then propagates to the adjacent areas. Beginning of the failure from the edges is due to the thermal stresses and the fast heating and cooling conditions at the edges of the specimens (Ref 16, 38). It can be noticed that the initial spallation thermal cycle of the as-sprayed and the laser-treated coating with dot, striation and grid is 43, 59, 55 and 43, respectively. After then, the spallation area of the as-sprayed coating increases obviously and the spallation tends to extend from edge to adjacent area. The as-sprayed specimen fails completely until 470 cycles (Fig. 8a). By contrast, the spallation rate of dotted specimen is very slow, and the dotted specimen fails after 960 thermal cycles as shown in Fig. 8(b). In this case, the spallation occurs between the outer edge of specimen and the dotted units. However, the striated and grid specimens show relatively short thermal cycle lifetimes. For the striated specimen, the spallation occurs at the edge of striated unit and then spreads along it. Eventually, the striated specimen fails after 205 thermal cycles (Fig. 8c). While the grid units have adverse effects on the thermal shock resistance of TBCs, the spallation occurs in the form of grid block. Consequently, the grid specimen fails after 130 thermal cycles (Fig. 8d).

The comparison of thermal cycling lifetimes between the as-sprayed and the laser-treated TBCs with different shapes is presented in Fig. 9. It can be seen that the dotted TBC exhibits an excellent average thermal cycling lifetime, approximately twice as much as that of the as-sprayed TBC. This is due to the fact that the columnar grains and segmented cracks in the dotted units are beneficial to increase the strain tolerance, thereby improving the thermal shock resistance (Ref 39, 40). However, the

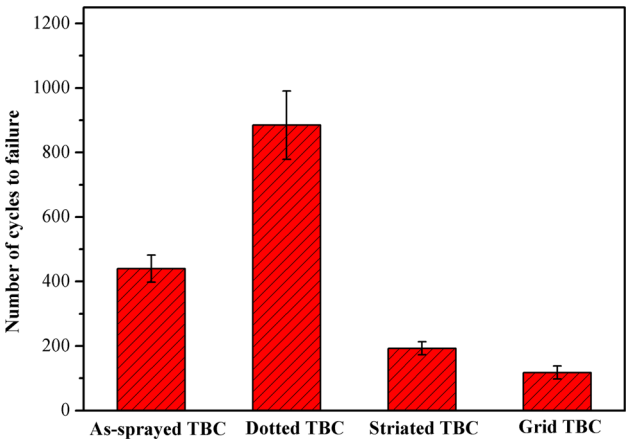


**Fig. 9** Thermal cycling lifetimes of the as-sprayed and laser-treated TBCs with different shapes

striated and grid units have adverse effects on the thermal shock resistance. Thermal shock resistance of the striated specimen decreases by 56%, while the thermal shock resistance of the grid specimen is the worst, which reduces by 73%.

Figure 10(a) shows XRD patterns of the as-sprayed and laser-treated TBCs with different shapes at the $2\theta$ range of 10°-90°. The phases of all coatings are mainly t′-$ZrO_2$ and c-$ZrO_2$ after thermal shock failure. There are no obvious diffraction peaks of m-$ZrO_2$ at the $2\theta$ range of 27.5°-32.5° in Fig. 10(b). That is to say, no m-$ZrO_2$ is detected in the as-sprayed and laser-treated TBCs with different shapes. Therefore, no phase transformation occurs in the as-sprayed and laser-treated TBCs during thermal shock tests. Consequently, the failure of the as-sprayed and laser-treated TBCs with different shapes is unaffected by the stresses stemming from phase transformation (Ref 17, 41).

Figure 11 shows the surface morphologies of the as-sprayed and the laser-treated specimens with different shapes after thermal shock test. The surface is much rougher, and there are many small pores and obvious tortuous microcracks on the surface of the as-sprayed TBC after thermal cycles shown in Fig. 11(a). This is a serious sintering phenomenon during the high-temperature service, which usually leads to the shrinkage on the surface of TBC and the increase in thermal mismatch between the coatings and the substrate. The thermal stress generated in the coating can be expressed by the following equation (Ref 42, 43):

$$\sigma_t = \Delta\alpha \Delta T E_c/(1-\upsilon_c) \quad \text{(Eq 1)}$$

where $\Delta\alpha$ is the difference of thermal expansion coefficient between the ceramic top coating and the substrate, $\Delta T$ is the temperature difference, $E_c$ and $\upsilon_c$ are the elastic modulus and the Poisson ratio of the coating, respectively. The sintering leads to an increase in elastic modulus which

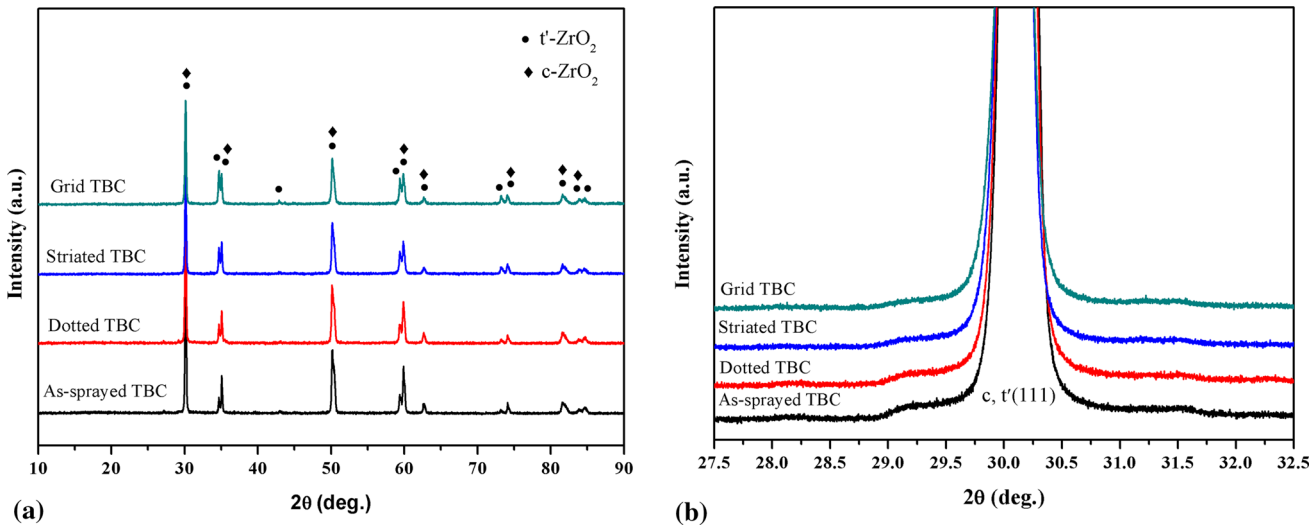


**Fig. 10** XRD patterns of the four coatings after thermal shock test: (a) 10°-90°, (b) 27.5°-32.5°

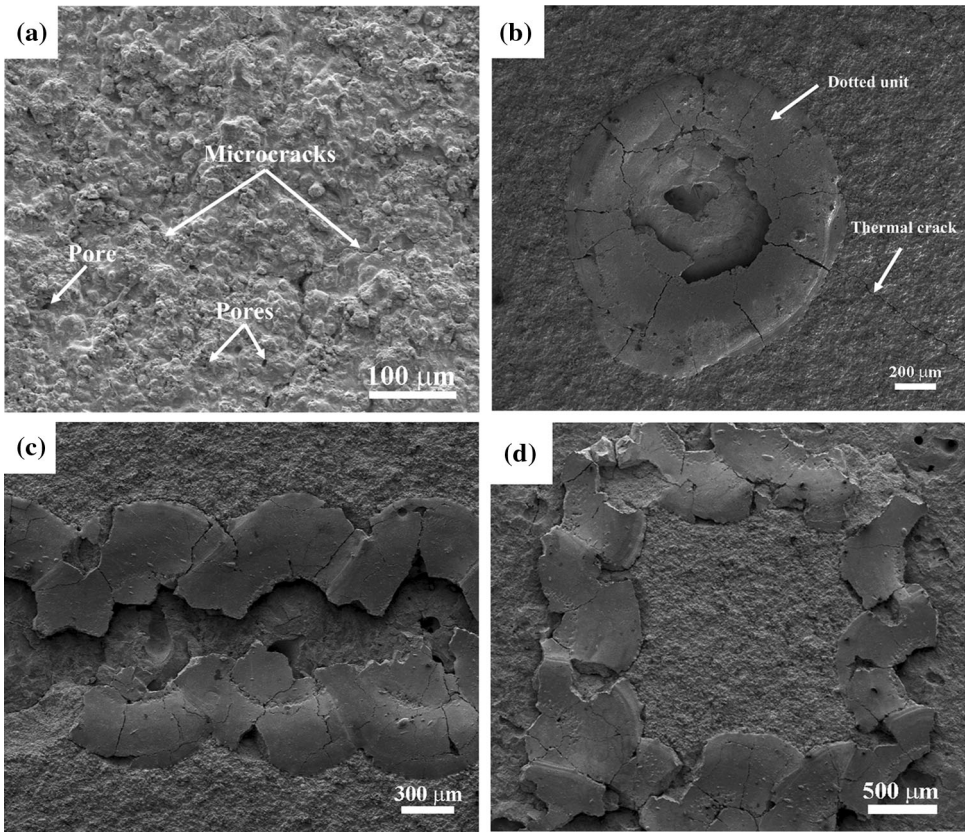


**Fig. 11** Surface morphologies of specimens after thermal shock test: (a) as-sprayed TBC, (b) dotted TBC, (c) striated TBC, and (d) grid TBC

decreases strain tolerance capability of the coating (Ref 44), thus increasing top coating stress according to Eq 1. This may eventually result in the spallation of TBCs. In addition, due to the intrinsic defects such as pores and voids in the ceramic top coating, the stress concentration would also promote the formation of microcracks. Many microcracks connect each other and gradually form a main crack, so the propagation of main crack is realized by bridge connections with microcracks in front of it, which finally causes the failure of the coatings under thermal cycles. Figure 11(b) shows the surface morphology of the dotted specimen after thermal shock test, and the center of the dotted unit spalls. It can be observed that further propagation pauses and it cannot traverse the unit

immediately when a thermal crack propagates to the dotted unit. There are multiple reasons for this. Firstly, due to the elimination of defects and the higher hardness of the laser-remelted zone, the resistance to crack propagation increases. Secondly, the columnar grains and segmented cracks in the dotted units can improve the strain tolerance. That is why the route of crack propagation can be shut by the dotted unit. However, the central area of the striated specimen is removed as shown in Fig. 11(c). By contrast, the spallation area of the grid TBC is the most among the specimens with three different shapes (Fig. 11d). Due to the early failure under short thermal cycles, thermal cracks were not found on the surface of the striated and grid specimens. As for the laser-treated specimens with dot, striation and grid, the area ratio of laser-treated zone shown in Table 3 is 18, 26 and 58%, respectively. In other words, the proportion of dense microstructure increases with the laser-treated area increasing. This may lead to the increase in elastic modulus (Ref 45). According to Eq 1, the thermal stress will increase. Therefore, the thermal stress of the grid specimen is greater than that of the striated specimen, and the thermal stress of the dotted specimen is the smallest. These are the reasons why the thermal shock resistance of the dotted specimen is the best and the grid specimen has worse thermal shock resistance than the striated specimen.

The cross-sectional morphologies of the as-sprayed and the laser-treated specimens with different shapes after thermal shock test are shown in Fig. 12. From Fig. 12(a), it can be seen that the surface of the top coating is rugged and there are some small transverse cracks and big pores inside the 7YSZ ceramic coating. And the TGO is formed at the interface between the top coating and the bond coating due to the oxygen penetration through the porosity of the ceramic layer. The average TGO thickness for the as-sprayed coating is about 2 μm. Due to the thermal expansion mismatch between the TGO layer and the NiCrAlY layer, large residual compressive stresses form in the TGO layer during the process of cooling to ambient temperature (Ref 46). During the subsequent thermal cycles, the release of stress occurs which is accompanied with tensile stresses parallel to TGO/YSZ interface (Ref 47), and this may aggravate the crack growth and propagation. Furthermore, the as-sprayed specimen failed with cracking and spallation of the TBC within the 7YSZ ceramic coating and away from the interface between the bond coating and the 7YSZ ceramic coating. Even though the dotted specimen experiences the longest thermal cycles, the dotted unit is still relatively complete after the thermal shock failure (Fig. 12b). Due to the columnar grains and vertical cracks in the dotted unit, it may allow better compliance of tensile stress through the free

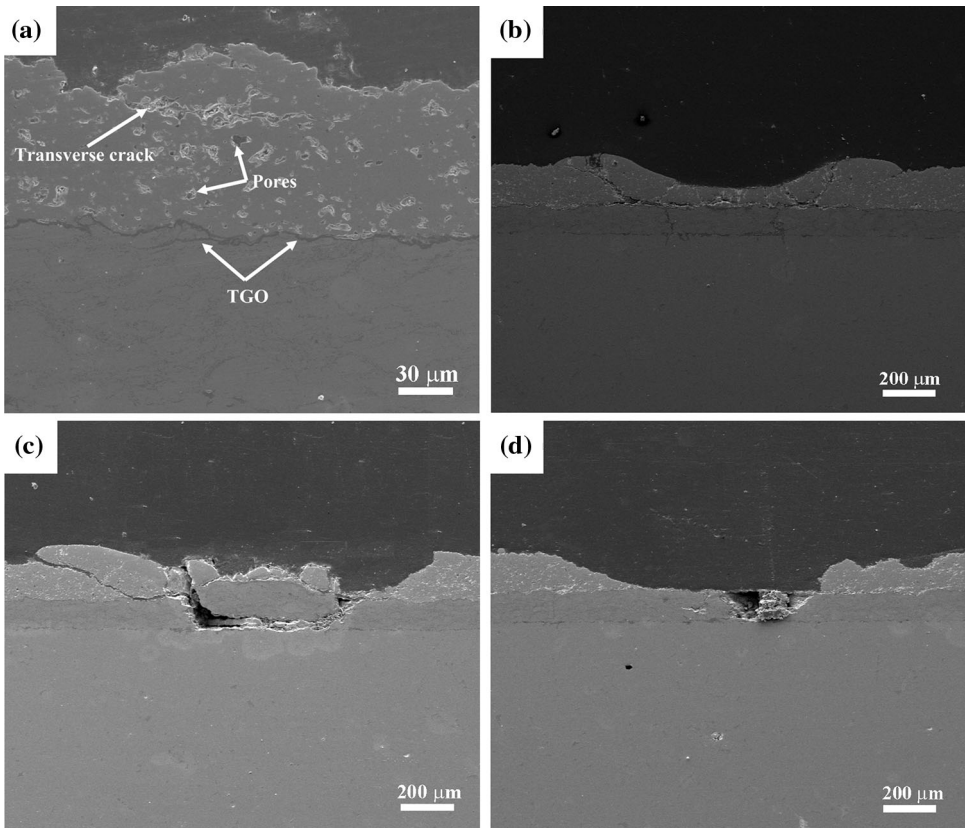


**Fig. 12** Cross section of (a) as-sprayed specimen, (b) dotted specimen, (c) striated specimen, and (d) grid specimen after thermal shock test

movement of individual columns. Therefore, it has excellent thermal shock resistance which can be attributed to the high stress absorption tendency in the coating when subjected to high-temperature thermal shock (Ref 18). However, the vertical cracks in the dotted unit may accelerate the formation of the TGO through oxygen rapid penetration during the later period of thermal shock test. Since the dotted unit experiences the 960 thermal cycles (Fig. 8b), the average thickness of TGO is about 3.7 μm. Figure 13 shows the EDS analysis of the dotted unit after thermal shock test. The elements Al and O are rich around the cracks and at the interface of top coating and bond coating. Accumulation of the TGO stress stimulates the propagation of microcracks at the interface between top coating and TGO. Moreover, the nearly transverse cracks around the unit (Fig. 6a) may propagate to the interface between top coating and bond coating with the thermal cycles increasing. With further connection between transverse cracks and vertical cracks, a part of dotted unit and the as-sprayed coating around it spall, which finally leads to the failure of the dotted specimen. By comparison, a half of the striated unit in the ceramic coating spalls and a part of the bond coating beneath the striated unit delaminates after the thermal shock failure (Fig. 12c). The grid unit in the ceramic coating spalls almost completely, and the partial bond coating beneath it delaminates, as shown in Fig. 12(d). It is well known that the laser processing is a process of transforming light energy into thermal energy. Due to the big overlapping area between the adjacent laser irradiation in the striated and grid specimens, the later

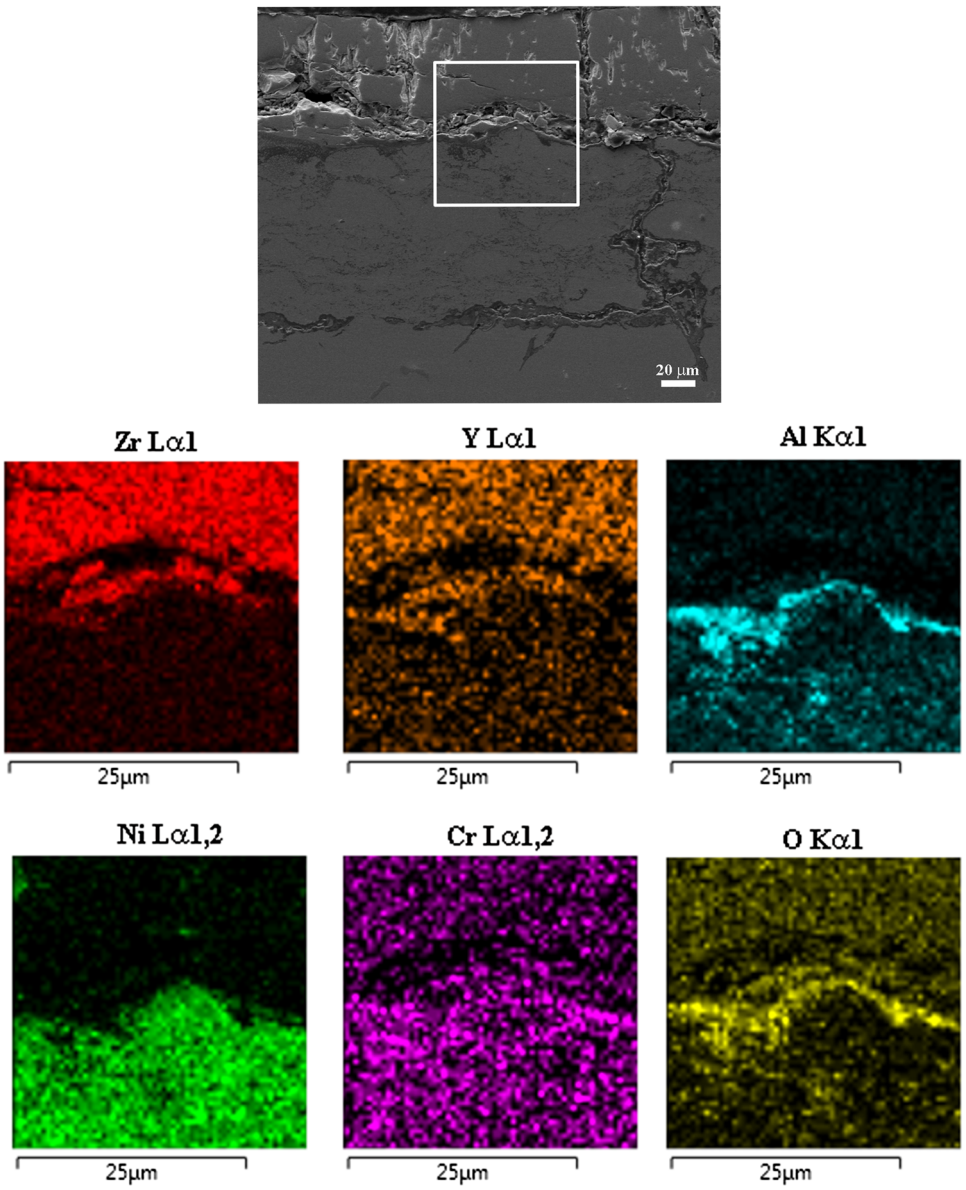


**Fig. 13** EDS analysis of the dotted unit after thermal shock failure

irradiation causes the reheating of the previous irradiation. Therefore, more thermal energy is absorbed in the laser-treated zone. Then, the heat is transferred from the coating to the substrate. In order to impede the shrinkage of the coating, the tensile stress is applied to the coating by the substrate (Ref 48). As a result, the striated and grid specimens present more continuous segmented cracks and transverse cracks, which deteriorate the thermal shock resistance conversely. Under the repeated heating and cooling cycles, on the one hand, the thermal expansion mismatch between metallic bond coating and ceramic top coating may induce the thermal stress. On the other hand, the formation of the TGO at the interface between the top coating and the bond coating can exert additional tensile stress on the YSZ surrounding the TGO. The average TGO thickness under the striated and grid units is approximately 0.9 and 0.5 μm, respectively. Since the striated and grid specimens early fail after 205 and 130 cycles (Fig. 8c and d), respectively, the as-sprayed specimen fails after 470 cycles (Fig. 8a). Therefore, the average TGO thickness of the striated and grid specimens is less than that of the as-sprayed specimen. With the increasing number of thermal cycles, the accumulated tensile stress may induce transverse cracks near the interface of metallic bond coating and ceramic top coating or the top coating and TGO. Further connection between transverse cracks and initial vertical cracks segregates the remelted coatings apart from the initial as-sprayed coatings, and partial bond coatings delaminate. This explains why the striated and grid specimens fail early and deteriorate the thermal shock resistance.

Figure 14 shows the diagrammatic sketch of the thermal shock failure of laser-treated specimens with different shapes. After the laser treatment, the segmented cracks are formed in the dotted unit (Fig. 14a). Furthermore, when a thermal crack from the as-sprayed coating propagates to the dotted unit, it stops and cannot traverse the unit. That is to say, the dotted unit can resist crack propagation, which finally prolongs the thermal cycles and improves the thermal shock resistance. However, the initial vertical cracks in the dotted unit may accelerate the formation of TGO during the later period of thermal shock test. Accumulation of the

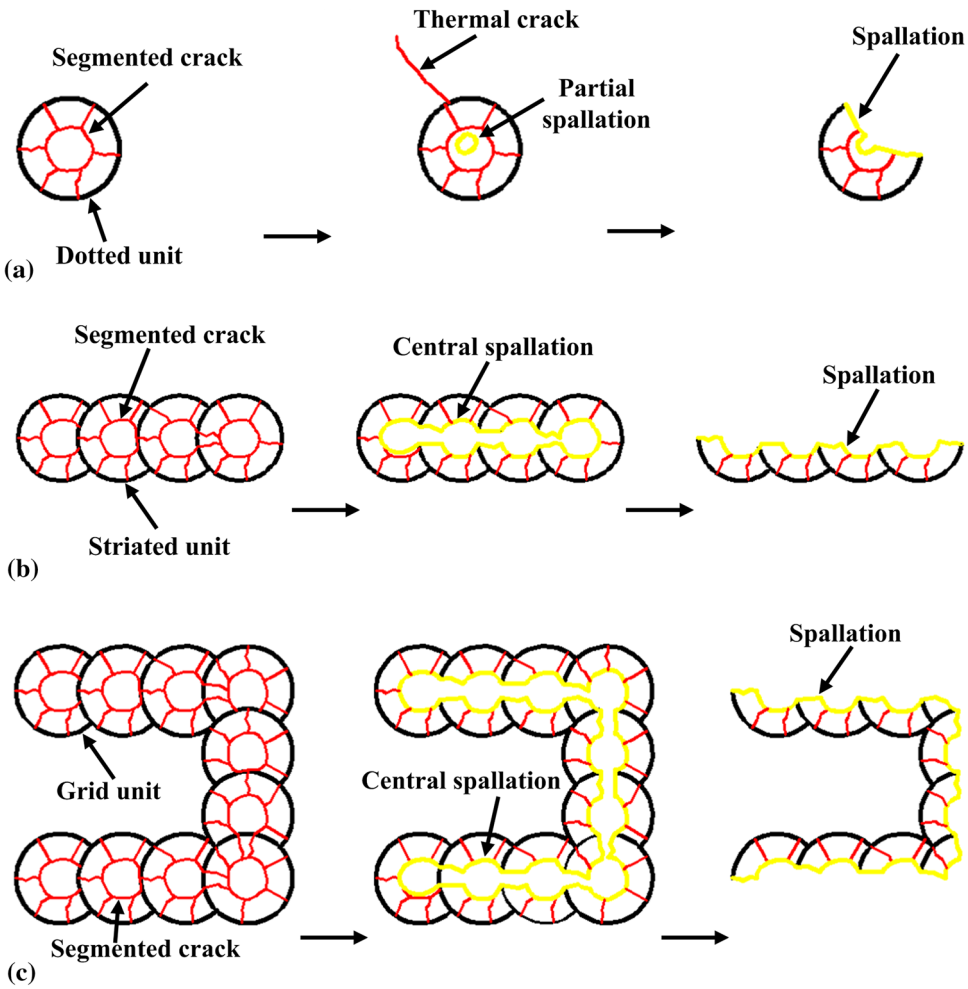


**Fig. 14** Diagrammatic sketch of the thermal shock failure of laser-treated specimens with different shapes: (a) the dotted specimen, (b) the striated specimen, and (c) the grid specimen

TGO stress stimulates the formation and propagation of transverse microcracks. Meanwhile, the nearly transverse cracks around the unit may further propagate. With the further connection between transverse cracks and vertical cracks, a part of dotted unit and the as-sprayed coating around it spall, which finally leads to the failure of the dotted specimen. For the striated and grid unit, due to the big overlapping area between the adjacent laser irradiation, the striated and grid specimens present more continuous segmented cracks and transverse cracks, as shown in Fig. 14(b) and (c). During the thermal shock test, on the one hand, some vertical cracks began to propagate and reach the top coating/TGO interface eventually. On the other hand, the formed TGO exerts tensile stress on the YSZ around it, which may promote the initiation and propagation of transverse cracks near the interface of the top coating and TGO. Furthermore, the transverse cracks connected with vertical cracks, and then the central area of the striated and grid units spalled. With the increase in thermal cycle, a half of the striated and grid units and the as-sprayed coating around them spall. This results in the early failure of striated and grid specimens.

## Conclusions

Inspired by the unique structures and shapes of biological organisms, the laser-treated specimens with different shapes were fabricated. The microstructure, microhardness, phase composition of units and the thermal shock resistance comparisons between the as-sprayed specimens and the laser-treated specimens with different shapes were studied systematically. And some important conclusions were drawn as follows:

1. The as-sprayed coating had the typical characteristic of lamellar structure, some pores and voids, microcracks, and protrusions. After the laser remelting process, the surface of the laser-remelted zone became smoother, the defects in the as-sprayed coating were eliminated, and the dense columnar crystal structure and the segmented cracks vertical to the surface were formed. Compared with the as-sprayed coating, the average microhardness of the laser-remelted zone was increased by 73%.
2. The thermal shock resistance of the dotted specimen was about twice that of the as-sprayed specimen. On the one hand, the existences of columnar grains and segmented cracks in the dotted unit allowed better strain tolerance under thermal cycles. On the other hand, the dotted unit could resist thermal crack propagation because of the elimination of defects and the higher hardness after laser remelting. Due to the improved thermal shock resistance and high process efficiency, the biomimetic laser remelting is an alternative approach to the industrial application of TBCs. Other performance of TBCs processed by this method will be explored in future work.
3. The striated and grid specimens exhibited worse thermal shock resistance than the as-sprayed specimen. Due to the big overlapping area, more continuous segmented cracks and transverse cracks were formed in the striated and grid units. Under the combined effect of thermal expansion mismatch stress and TGO stress, connection between transverse cracks and initial vertical cracks segregated the remelted zone apart from the initial as-sprayed coatings. Finally, the striated and grid specimens failed early.

**Acknowledgments** This work is supported by Guangdong Province Science and Technology Plan Projects (2016A030312015, 2017A070702016, 2017B030314122 and 2017A070701027), Guangzhou Project of Science and Technology (201807010030), Zhongshan Project of Science and Technology (2017G1FC0008), Natural Science Foundation of Guangdong Province (2016A030312015), the National Natural Science Foundation for Youth (51501044) and GDAS' Project of Science and Technology Development (2018GDASCX-0111, 2017GDASCX-0202, 2017GDASCX-0111 and 2018GDASCX-0402).

## References

1. C.J. Li, Y. Li, G.J. Yang, and C.X. Li, A Novel Plasma-Sprayed Durable Thermal Barrier Coating with a Well-Bonded YSZ Interlayer Between Porous YSZ and Bond Coat, *J. Therm. Spray Technol.*, 2012, **21**(3-4), p 383-390
2. C.B. Liu, Z.M. Zhang, X.L. Jiang, M. Liu, and Z.H. Zhu, Comparison of Thermal Shock Behaviors Between Plasma-Sprayed Nanostructured and Conventional Zirconia Thermal Barrier Coatings, *Trans. Nonferr. Met. Soc.*, 2009, **19**(1), p 99-107
3. G.H. Meng, B.Y. Zhang, H. Liu, G.J. Yang, T. Xu, C.X. Li, and C.J. Li, Highly Oxidation Resistant and Cost Effective MCrAlY Bond Coats Prepared by Controlled Atmosphere Heat Treatment, *Surf. Coat. Technol.*, 2018, **347**, p 54-65
4. A. Rico, J. Gomez-Garcia, C.J. Munez, P. Poza, and V. Utrilla, Mechanical Properties of Thermal Barrier Coatings After Isothermal Oxidation. Depth Sensing Indentation Analysis, *Surf. Coat. Technol.*, 2009, **203**(16), p 2307-2314
5. M. Daroonparvar, M.A.M. Yajid, N.M. Yusof, S. Farahany, M.S. Hussain, H.R. Bakhsbeshi-Rad, Z. Valefi, and A. Abdolahi, Improvement of Thermally Grown Oxide Layer in Thermal Barrier Coating Systems with Nano Alumina as Third Layer, *Trans. Nonferr. Met. Soc.*, 2013, **23**(5), p 1322-1333
6. Y.Q. Wang and G. Sayre, Commercial Thermal Barrier Coatings with a Double-Layer Bond Coat on Turbine Vanes and the Process Repeatability, *Surf. Coat. Technol.*, 2009, **203**(16), p 2186-2192
7. X.R. Ren, M. Zhao, J. Feng, and W. Pan, Phase Transformation Behavior in Air Plasma Sprayed Yttria Stabilized Zirconia Coating, *J. Alloys Compd.*, 2018, **750**, p 189-196
8. X.F. Zhang, K.S. Zhou, M. Liu, C.M. Deng, C.G. Deng, J.B. Song, and X. Tong, Enhanced Properties of Al-Modified EB-PVD 7YSZ Thermal Barrier Coatings, *Ceram. Int.*, 2016, **42**(12), p 13969-13975
9. A.D. Jadhav, N.P. Padture, E.H. Jordan, M. Gell, P. Miranzo, and E.R. Fuller, Low-Thermal-Conductivity Plasma-Sprayed

Thermal Barrier Coatings with Engineered Microstructures, *Acta Mater.*, 2006, **54**(12), p 3343-3349
10. F.F. Zhou, Y. Wang, L. Wang, Z.Y. Cui, and Z.G. Zhang, High Temperature Oxidation and Insulation Behavior of Plasma-Sprayed Nanostructured Thermal Barrier Coatings, *J. Alloys Compd.*, 2017, **704**, p 614-623
11. F.F. Zhou, Y. Wang, L. Wang, Y.M. Wang, W.L. Chen, C.X. Huang, and M. Liu, Synthesis and Characterization of Nanostructured t′-YSZ Spherical Feedstocks for Atmospheric Plasma Spraying, *J. Alloys Compd.*, 2018, **740**, p 610-616
12. Q.Z. Cui, S.M. Seo, Y.S. Yoo, Z. Lu, S.W. Myoung, Y.G. Jung, and U. Paik, Thermal Durability of Thermal Barrier Coatings with Bond Coat Composition in Cyclic Thermal Exposure, *Surf. Coat. Technol.*, 2015, **284**, p 69-74
13. H. Dong, G.J. Yang, H.N. Cai, H. Ding, C.X. Li, and C.J. Li, The Influence of Temperature Gradient Across YSZ on Thermal Cyclic Lifetime of Plasma-Sprayed Thermal Barrier Coatings, *Ceram. Int.*, 2015, **41**(9), p 11046-11056
14. M.R. Begley and H.N.G. Wadley, Delamination Resistance of Thermal Barrier Coatings Containing Embedded Ductile Layers, *Acta Mater.*, 2012, **60**(6-7), p 2497-2508
15. X.H. Zhong, H.Y. Zhao, C.G. Liu, L. Wang, F. Shao, X.M. Zhou, S.Y. Tao, and C.X. Ding, Improvement in Thermal Shock Resistance of Gadolinium Zirconate Coating by Addition of Nanostructured Yttria Partially-Stabilized Zirconia, *Ceram. Int.*, 2015, **41**(6), p 7318-7324
16. Z. Soleimanipour, S. Baghshahi, and R. Shoja-razavi, Improving the Thermal Shock Resistance of Thermal Barrier Coatings Through Formation of an In Situ YSZ/$Al_2O_3$ Composite via Laser Cladding, *J. Mater. Eng. Perform.*, 2017, **26**(4), p 1890-1899
17. R. Ghasemi, R. Shoja-Razavi, R. Mozafarinia, and H. Jamali, The Influence of Laser Treatment on Thermal Shock Resistance of Plasma-Sprayed Nanostructured Yttria Stabilized Zirconia Thermal Barrier Coatings, *Ceram. Int.*, 2014, **40**(1), p 347-355
18. Z.J. Fan, K.D. Wang, X. Dong, W.Q. Duan, X.S. Mei, W.J. Wang, J.L. Cui, and J. Lv, Influence of Columnar Grain Microstructure on Thermal Shock Resistance of Laser Re-melted $ZrO_2$-7 wt% $Y_2O_3$ Coatings and Their Failure Mechanism, *Surf. Coat. Technol.*, 2015, **277**, p 188-196
19. J.H. Lee, P.C. Tsai, and C.L. Chang, Microstructure and Thermal Cyclic Performance of Laser-Glazed Plasma-Sprayed Ceria-Yttria-Stabilized Zirconia Thermal Barrier Coatings, *Surf. Coat. Technol.*, 2008, **202**(22-23), p 5607-5612
20. J.Y. Sun, J. Tong, and Y.H. Ma, Nanomechanical Behaviours of Cuticle of Three Kinds of Beetle, *J. Bionic Eng.*, 2008, **5**, p 152-157
21. J. Lomakin, Y. Arakane, K.J. Kramer, R.W. Beeman, M.R. Kanost, and S.H. Gehrke, Mechanical Properties of Elytra from Tribolium Castaneum Wild-Type and Body Color Mutant Strains, *J. Insect Physiol.*, 2010, **56**(12), p 1901-1906
22. T.R. Faisal, E.M.K. Abad, N. Hristozov, and D. Pasini, The Impact of Tissue Morphology, Cross-Section and Turgor Pressure on the Mechanical Properties of the Leaf Petiole in Plants, *J. Bionic Eng.*, 2010, **7**, p S11-S23
23. X.S. Wang, Y. Li, and Y.F. Shi, Effects of Sandwich Microstructures on Mechanical Behaviors of Dragonfly Wing Vein, *Compos. Sci. Technol.*, 2008, **68**(1), p 186-192
24. H. Zhou, L. Chen, W. Wang, L.Q. Ren, H.Y. Shan, and Z.H. Zhang, Abrasive Particle Wear Behavior of 3Cr2W8V Steel Processed to Bionic Non-smooth Surface by Laser, *Mat. Sci. Eng. A Struct.*, 2005, **412**(1-2), p 323-327
25. H. Zhou, N. Sun, H.Y. Shan, D.Y. Ma, X. Tong, and L.Q. Ren, Bio-inspired Wearable Characteristic Surface: Wear Behavior of Cast Iron with Biomimetic Units Processed by Laser, *Appl. Surf. Sci.*, 2007, **253**(24), p 9513-9520
26. X. Tong, H. Zhou, Z.H. Zhang, N. Sun, H.Y. Shan, and L.Q. Ren, Effects of Surface Shape on Thermal Fatigue Resistance of Biomimetic Non-smooth Cast Iron, *Mater. Sci. Eng. A Struct.*, 2007, **467**(1-2), p 97-103
27. J.R. Song, C.C. Fan, H.S. Ma, L.H. Liang, and Y.G. Wei, Crack Deflection Occurs by Constrained Microcracking in Nacre, *Acta Mech. Sinica Prc.*, 2018, **34**(1), p 143-150
28. Z.H. Zhang, L. Zhang, Z.L. Yu, J.J. Liu, X.J. Li, and Y.H. Liang, In-Situ Mechanical Test of Dragonfly Wing Veins and Their Crack Arrest Behavior, *Micron*, 2018, **110**, p 67-72
29. F. Nozahic, D. Monceau, and C. Estournes, Thermal Cycling and Reactivity of a $MoSi_2/ZrO_2$ Composite Designed for Self-Healing Thermal Barrier Coatings, *Mater. Des.*, 2016, **94**, p 444-448
30. A.K. Ray and R.W. Steinbrech, Crack Propagation Studies of Thermal Barrier Coatings Under Bending, *J. Eur. Ceram. Soc.*, 1999, **19**(12), p 2097-2109
31. F. Chang, K.S. Zhou, X. Tong, L.P. Xu, X.F. Zhang, and M. Liu, Microstructure and Thermal Shock Resistance of the Peg-Nail Structured TBCs Treated by Selective Laser Modification, *Appl. Surf. Sci.*, 2014, **317**, p 598-606
32. F.F. Zhou, Y. Wang, Z.Y. Cui, L. Wang, J.F. Gou, Q.W. Zhang, and C.H. Wang, Thermal Cycling Behavior of Nanostructured 8YSZ, SZ/8YSZ and 8CSZ/8YSZ Thermal Barrier Coatings Fabricated by Atmospheric Plasma Spraying, *Ceram. Int.*, 2017, **43**(5), p 4102-4111
33. S.R. Dhineshkumar, M. Duraiselvam, S. Natarajan, S.S. Panwar, T. Jena, and M.A. Khan, Enhancement of Strain Tolerance of Functionally Graded $LaTi_2Al_9O_{19}$ Thermal Barrier Coating Through Ultra-short Pulse Based Laser Texturing, *Surf. Coat. Technol.*, 2016, **304**, p 263-271
34. C. Batista, A. Portinha, R.M. Ribeiro, V. Teixeira, M.F. Costa, and C.R. Oliveira, Surface Laser-Glazing of Plasma-Sprayed Thermal Barrier Coatings, *Appl. Surf. Sci.*, 2005, **247**(1-4), p 313-319
35. L. Wang, X.H. Zhong, F. Shao, J.X. Ni, J.S. Yang, S.Y. Tao, and Y. Wang, What is the Suitable Segmentation Crack Density for Atmospheric Plasma Sprayed Thick Thermal Barrier Coatings with the Improved Thermal Shock Resistance?, *Appl. Surf. Sci.*, 2018, **431**, p 101-111
36. G.R. Li, G.J. Yang, C.X. Li, and C.J. Li, Strain-Induced Multiscale Structural Changes in Lamellar Thermal Barrier Coatings, *Ceram. Int.*, 2017, **43**(2), p 2252-2266
37. P.P. Zhang, F.H. Li, X.F. Zhang, Z.H. Zhang, C.L. Tan, L.Q. Ren, Y.L. Wang, W.Y. Ma, and M. Liu, Effect of Bionic Unit Shapes on Solid Particle Erosion Resistance of $ZrO_2$-7 wt%$Y_2O_3$ Thermal Barrier Coatings Processed by Laser, *J. Bionic Eng.*, 2018, **15**(3), p 545-557
38. H. Jamali, R. Mozafarinia, R.S. Razavi, and R. Ahmadi-Pidani, Comparison of Thermal Shock Resistances of Plasma-Sprayed Nano Structured and Conventional Yttria Stabilized Zirconia Thermal Barrier Coatings, *Ceram. Int.*, 2012, **38**(8), p 6705-6712
39. I. Sevostianov and M. Kachanov, Elastic and Conductive Properties of Plasma-Sprayed Ceramic Coatings in Relation to Their Microstructure: An Overview, *J. Therm. Spray Technol.*, 2009, **18**(5-6), p 822-834
40. Y. Bai, Z.H. Han, H.Q. Li, C. Xu, Y.L. Xu, Z. Wang, C.H. Ding, and J.F. Yang, High Performance Nanostructured $ZrO_2$ Based Thermal Barrier Coatings Deposited by High Efficiency Supersonic Plasma Spraying, *Appl. Surf. Sci.*, 2011, **257**(16), p 7210-7216
41. R. Ahmadi-Pidani, R. Shoja-Razavi, R. Mozafarinia, and H. Jamali, Evaluation of Hot Corrosion Behavior of Plasma Sprayed Ceria and Yttria Stabilized Zirconia Thermal Barrier Coatings in the Presence of $Na_2SO_4 + V_2O_5$ Molten Salt, *Ceram. Int.*, 2012, **38**(8), p 6613-6620
42. M.J. Lee, B.C. Lee, J.G. Lim, and M.K. Kim, Residual Stress Analysis of the Thermal Barrier Coating System by Considering

the Plasma Spraying Process, *J. Mech. Sci. Technol.*, 2014, **28**(6), p 2161-2168
43. J.S. Wang, J.B. Sun, H. Zhang, S.J. Dong, J.N. Jiang, L.H. Deng, X. Zhou, and X.Q. Cao, Effect of Spraying Power on Microstructure and Property of Nanostructured YSZ Thermal Barrier Coatings, *J. Alloys Compd.*, 2018, **730**, p 471-482
44. J. Wu, H.B. Guo, Y.Z. Gao, and S.K. Gong, Microstructure and Thermo-Physical Properties of Yttria Stabilized Zirconia Coatings with CMAS Deposits, *J. Eur. Ceram. Soc.*, 2011, **31**(10), p 1881-1888
45. X.C. Zhang, M. Watanabe, and S. Kuroda, Effects of Processing Conditions on the Mechanical Properties and Deformation Behaviors of Plasma-Sprayed Thermal Barrier Coatings: Evaluation of Residual Stresses and Mechanical Properties of Thermal Barrier Coatings on the Basis of In Situ Curvature Measurement Under a Wide Range of Spray Parameters, *Acta Mater.*, 2013, **61**(4), p 1037-1047
46. A.G. Evans, D.R. Mumm, J.W. Hutchinson, G.H. Meier, and F.S. Pettit, Mechanisms Controlling the Durability of Thermal Barrier Coatings, *Prog. Mater Sci.*, 2001, **46**(5), p 505-553
47. A.N. Khan and J. Lu, Behavior of Air Plasma Sprayed Thermal Barrier Coatings, Subject to Intense Thermal Cycling, *Surf. Coat. Technol.*, 2003, **166**(1), p 37-43
48. Y. Wang, G. Darut, X.T. Luo, T. Poirier, J. Stella, H.L. Liao, and M.P. Planche, Influence of Preheating Processes on the Microstructure of Laser Glazed YSZ Coatings, *Ceram. Int.*, 2017, **43**(5), p 4606-4611